

Proton dynamics in high-pressure ice-VII from density functional theory

Florian Trybel,^{1,*} Michael Cosacchi,² Thomas Meier,¹ Vollrath Martin Axt,² and Gerd Steinle-Neumann¹

¹*Bayerisches Geoinstitut, Universität Bayreuth, D-95440 Bayreuth, Germany*

²*Theoretische Physik III, Universität Bayreuth, D-95440 Bayreuth, Germany*

(Dated: March 19, 2022)

Using a density-functional-theory-based approach, we explore the symmetrization and proton dynamics in ice-VII, for which recent high-pressure NMR experiments indicate significant proton dynamics in the pressure-range of 20 – 95 GPa. We directly sample the potential seen by the proton and find a continuous transition from double- to single-well character over the pressure range of 2 to 130 GPa accompanied by proton dynamics in agreement with the NMR experiments.

I. INTRODUCTION

The discovery of ice-VII inclusions in diamonds from the Earth's mantle¹ highlights the importance of this high-pressure phase of water for planetary interiors beyond the icy satellites of Jupiter and Saturn in our solar system^{2,3}, and potentially H₂O-dominated exosolar planets^{4,5}. At room temperature (T), water crystallizes as ice-VII at pressures (P) above 2 GPa in a cubic structure (spacegroup $Pn\bar{3}m$), based on a body centered cubic (bcc) arrangement of oxygens with two possible proton positions along the diagonal O-O direction (dOod) that are occupied randomly (Fig. 1), but assumed to follow the ice rules: Each oxygen atom is covalently bound to two hydrogen atoms and each resulting water-like unit forms two hydrogen bonds to other oxygen atoms⁷. With increasing P , the O-H...O bond continuously symmetrizes to form ice-X, a process that has been of great interest in high- P physics and chemistry^{8–25}. In ice-VII a double-well potential along the O-O direction can be found under correlated proton movement^{14,21} which changes significantly under compression. This double-well potential provides the basis for understanding the proton dynamics, recently observed with nuclear magnetic resonance (NMR) experiments in the diamond anvil cell²⁶. Although numerous studies have investigated the properties of high- P ice-VII for more than 35 years⁸, no consensus on the symmetrization P has emerged. Proton dynamics and the underlying potential have been calculated from computationally expensive path-integral based simulations at individual P conditions only²¹ (Drechsel-Grau and Marx²⁷ for hexagonal ice), or indirectly from density-functional-theory (DFT) based approaches^{16,18,20,25}.

Using Kohn-Sham (KS) DFT, we trace the potential by displacing all, six and a single proton along dOod to investigate proton dynamics and explore symmetrization under compression.

II. DFT-SIMULATIONS

All KS-DFT-based calculations are performed with QUANTUM ESPRESSO 6.1^{39,40}, where possible using GPU-acceleration⁴¹. We combine the optBK88-

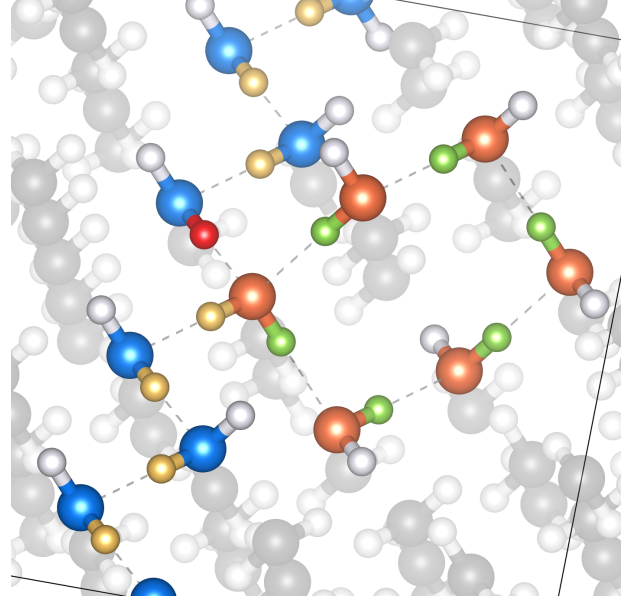


FIG. 1. Cut through the 4x4x4 ice-VII supercell. The sampling of the correlated hexagonal configuration is performed by moving the green protons in the ring of orange oxygen atoms. For the single proton sampling, the red proton is moved. To provide local charge neutrality, the ice-rule violating defects for the OH⁻ and H₃O⁺ configurations are moved to the edge of the simulations cell, along a path similar to that outlined by the golden hydrogen atoms. VESTA 3⁵² is used for structural visualizations.

vdW^{42–48} approximation to exchange and correlation, found most suitable for various water properties⁴⁹, with projector augmented wave atomic files for H and O based on the Perdew-Burke-Ernzerhof⁵⁰ exchange-correlation approximation (1s electrons treated as semi-relativistic core states for O). Convergence tests with a threshold of 10⁻⁴ Ry lead to a Monkhorst-Pack k-point grid⁵¹ of 1×1×1 for the 384 atom cells and a cutoff energy for plane wave expansion of 130 Ry.

III. PROTON POTENTIALS

We build ice-VII cells with 384 atoms (lattice constants between $l = 3.35$ Å and 2.55 Å), following the ice

rules⁷. All protons are simultaneously moved by the same amount along the respective O-O diagonal (22 steps), calculated energies are interpolated with a third-order spline, and the optimal proton position at each l is determined. We obtain a double-well potential (characterized by an energy barrier Φ_m and the distance between minimum location and the center of the O-O diagonal, δ_c) at low compression (Fig. 2), and we observe a continuous transition to a single well with decreasing l (Fig. S1 in the Supp. Mat.⁶). In the following, the optimized proton position from the collective displacement of all protons at the respective l is used as the reference position, when only some protons are considered.

Moving a single proton along dOOD in the ice-rule conforming cell (red atom in Fig. 1) leads to an asymmetric single-well potential, with the minimum corresponding to one of the minima in the double well obtained from

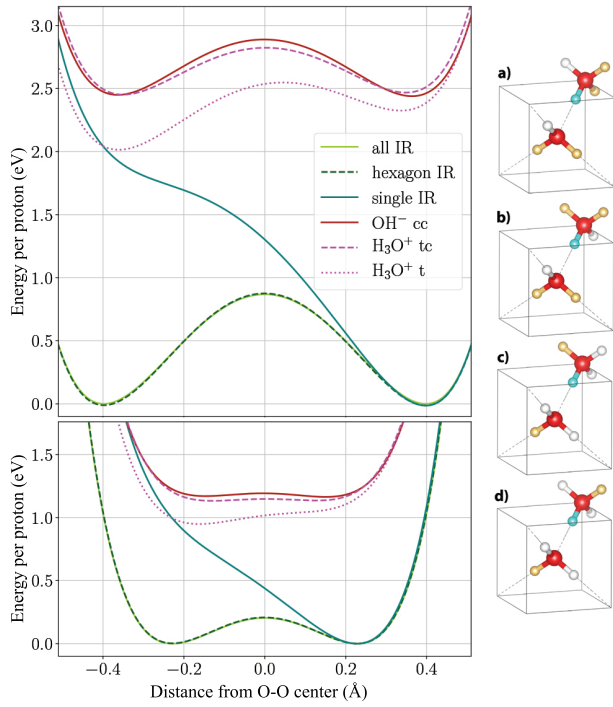


FIG. 2. Energy of different proton configurations for $l = 3.35$ Å (**top**) and $l = 2.95$ Å (**bottom**) and **a-d**) visualization of possible configurations with a single-proton ice-rule (IR) violation: Oxygen is shown in red, unoccupied hydrogen positions in white, occupied hydrogen positions in yellow and sampled hydrogen in blue: **a**) H_3O^+ in cis configuration (cis- H_3O^+), **b**) trans- H_3O^+ , **c**) cis- OH^- and **d**) trans- OH^- . Potentials displayed are for the collective motion of protons (all), the collective hexagonal configuration (hexagon) and a single proton (single), all obeying IR. Potentials for the IR-breaking arrangements are trans- H_3O^+ (t), without and with conjugation (tc) of the associated charge defect, and cis- OH^- in the conjugated configuration (cc). Conjugated trans- H_3O^+ and conjugated cis- OH^- are shown as they bracket the potential of all conjugated IR-breaking structures.

the collective displacement of all protons (Fig. 2), which – once the double-well character is lost – converges to a symmetric potential (Fig. S2 in the Supp. Mat.⁶).

In previous path-integral-based studies²¹, a collective motion of six protons in a hexagonal configuration was identified without breaking the ice rules. We follow this suggestion and move six protons in such a configuration (green atoms in Fig. 1), while the others remain at the optimized position for the respective l . We obtain potentials almost perfectly corresponding to the all-proton case in terms of energy/proton (Fig. 2), with the double-well character steadily decreasing with decreasing l (Fig. 3). Under further compression, the high- P single-well becomes increasingly localized (Fig. S3 in the Supp. Mat.⁶). The potentials show a slight asymmetry caused by the non-central position of the hexagon in the simulation cell in combination with periodic boundary conditions.

By breaking the ice rules, it is possible to create environments in which a single proton experiences a double-well potential when moved along the O-O diagonal. Four different cases of ice-rule breaking configurations (Fig. 2) can be distinguished based on the oxygen-proton ratio, OH^- (Fig. 2 c,d) and H_3O^+ (Fig. 2 a,b), and different configuration, i.e., (rotational) symmetry: (pseudo-)cis with protons aligned along dOOD (Fig. 2 a,c), and trans with protons facing each other (Fig. 2 b,d). Due to violation of local charge neutrality, the potentials of all OH^- and H_3O^+ configurations are higher in energy and asymmetric, as illustrated explicitly for trans- H_3O^+ in Fig. 2. To mitigate the asymmetry, we conjugate the charge defect along a path of water molecules (golden atoms in Fig. 1) to the edge of the simulation cell to minimize its influence (Figs. S4 and S5 in the Supp. Mat.⁶). The violation of the ice rules⁷ introduces an energy difference of $\simeq 2$ eV at $l = 3.35$ Å (Fig. 2), which decreases with compression. Restoring local charge neutrality at the sampling point as described earlier, leads to a small increase of the shift by $\simeq 0.05$ eV (Fig. 2).

Comparing δ_c and Φ_m for all six cases discussed above (Fig. 3), we find a splitting into two groups: Ice-rule violating structures lose the double-well character at a smaller compression, $l \lesssim 2.8 - 2.85$ Å, compared to the ice-rule conforming structures, with $l \lesssim 2.675$ Å.

Nevertheless, the functional behavior of both parameters with compression, expressed in terms of lattice parameter l , is similar for all cases - following a quadratic function for Φ_m and a square root for δ_c (Fig. 3). Comparing the double-well potential from the path-integral simulations by Lin *et al.*²¹ with our results, their δ_c is in very good agreement with the hexagonal configuration; Φ_m is larger in our calculations, with the difference most likely caused by theirs being ensemble calculations in contrast to our individual configuration approach and – more importantly – the classical treatment of protons in our calculations to this point.

Temperature has been neglected in the evaluation of the potentials. As we create unstable configurations during

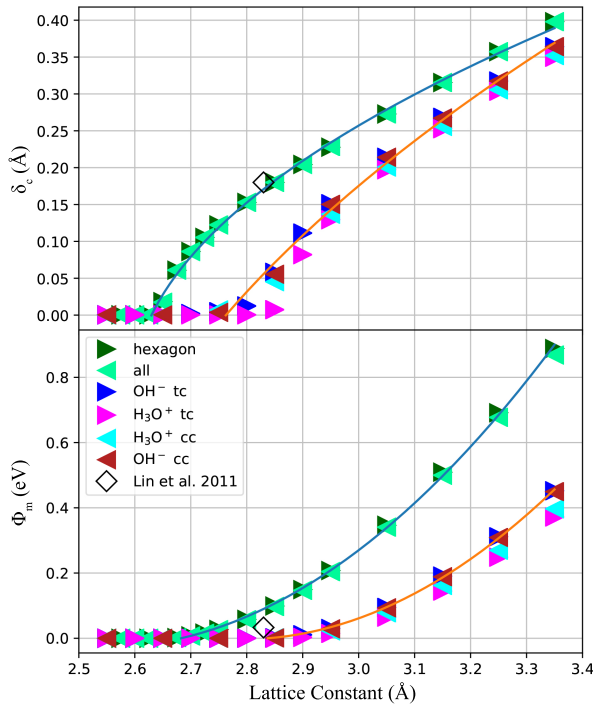


FIG. 3. Parameters describing the structure of the double-well potential as a function of lattice parameter l . **(top)** δ_c , the distance between the center of the double well and the minima. **(bottom)** Φ_m , the height of the barrier. Solid lines are fits of a square root for δ_c and a quadratic function for Φ_m to the hexagonal (green, $\Phi_m^{\text{Hex}} = 1.42(x - 2.54)^2$, $\delta_c^{\text{Hex}} = 0.57(x - 2.59)^{0.5} - 0.10$) and trans- OH^- points (orange, $\Phi_m^{\text{OH}^- \text{tc}} = 1.46(x - 2.79)^2$, $\delta_c^{\text{OH}^- \text{tc}} = 0.90(x - 2.49)^{0.5} - 0.46$). Open black diamonds show result of path integral *ab-initio* molecular dynamics simulations at $l = 2.84 \text{ \AA}$.²¹

sampling, harmonic lattice dynamics simulations would show negative phonon modes, and in molecular dynamics the structure would fall back to an equilibrium. The good agreement between the path integral results²¹ and our calculations with respect to δ_c suggests that vibrational effects do not influence the width of the potential significantly. By evaluating results as a function of l and not P , thermal expansion does not influence the outcome. In order to compare to experimental data, we use the thermal equation of state by French and Redmer²² to transform l to P at 300 K.

IV. PROTON DYNAMICS

Many high- P techniques do not provide access to the potential itself, but the electron density close to the protons by X-rays^{12,15,28,29}, and the response of the lattice to an excitation of phonon modes by Raman/infrared^{10,12,30–32} or Brillouin¹⁹ spectroscopy

can be measured at high P . High- P NMR spectroscopy, by contrast, enables the investigation of effective proton dynamics²⁶ by performing a line-shape analysis.

A. Ansatz

In order to compare with the latter results, we use a matrix exponential formalism to solve the time (t) dependent Schrödinger equation for a wave packet in the respective one-dimensional potentials obtained from the DFT-based sampling (see Supp. Mat.⁶ for details). The initial state is described by a generic 1D-Gaussian of the form

$$\Psi = \mathcal{I}^{-1} \cdot \mathcal{F}\left(\frac{x - x_0}{3a}\right) \cdot \frac{1}{\sqrt{a\sqrt{\pi}}} \exp\left(-0.5\left(\frac{x - x_0}{a}\right)^2\right), \quad (1)$$

where \hbar is the reduced Planck constant, x the position along dOOD, a and x_0 the width and center of the Gaussian, m the proton mass; \mathcal{I} ensures normalization and \mathcal{F} is a mollifier³³, improving the localization of Ψ , which leads to a significant speed-up and higher stability of the numerics, without affecting any physical features.

We assume that through spontaneous symmetry breaking the protons are located at one of the minima at t_0 and we therefore choose the initial state such that x_0 coincides with one of the minima of the potential for each l .

An eigenvalue analysis of the Hamiltonian is helpful to understand the idea behind this choice with respect to the analysis of effective single-particle dynamics and the spectral features. If we construct the initial state as a superposition of the two lowest eigenstates, it is straightforward to show that the resulting wave packet oscillates between the minima with a frequency exactly corresponding to the difference in energies of both eigenstates (ν_{01}^H), representing tunnelling. As the eigenstates of the Hamiltonian are a basis set, any initial state can be decomposed into them, and the resulting dynamics includes all frequencies (ν^H) which correspond to the combinatorically possible differences between their energies. While exactly diagonalizing the Hamiltonian yields all ν^H taking part in the dynamics, solving the problem with a physically motivated initial state additionally provides access to amplitudes.

We calculate the t -evolution of Ψ with respect to the potentials of the hexagonal as well as the four ice-rule violating configurations³⁴. In each t -step, the probability of finding the proton in the left half of the double-well potential is given by (Fig. 4)

$$p(x < 0) = \int_{-\infty}^0 |\Psi(x)|^2 dx. \quad (2)$$

The Fourier transform of $p(x < 0)$, $p(k)$, results in a ν^{FT} -spectrum that perfectly coincides with the transitions based on the Hamiltonian (Fig. 5 for the hexagonal configuration), which can be seen as a check for the solver, in addition to energy and norm conservation.

Choosing x_0 for the initial state as the minimum of the respective potential leads to a non-zero overlap between the ground state and the first excited state and therefore $\nu_{01}^{FT} > 0$ as long as x_0 is not central. Once the minimum of the potential, and consequently x_0 , is at the center of dOOD, no overlap between the ground state (symmetric) and the first excited state (antisymmetric) is expected, and the amplitude of ν_{01}^{FT} should vanish, indicating the completion of symmetrization.

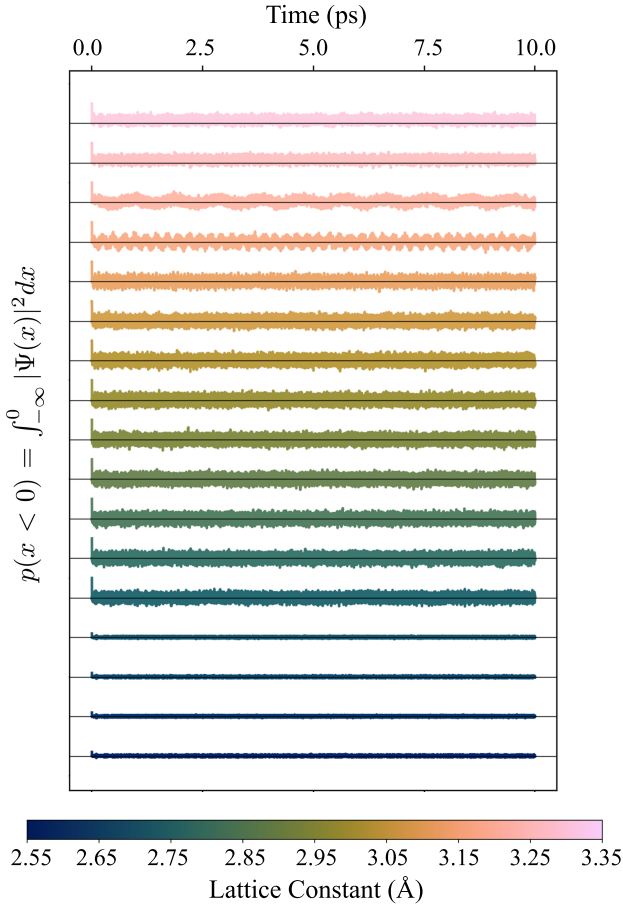


FIG. 4. Probability of finding the proton in the left half of the potential ($p(x < 0)$) as a function of time for the hexagonal configuration. Black lines indicate $p(x < 0) = 0.5$. For $l \geq 3.25$ Å, $p(x < 0) \gtrsim 0.5$ by construction. With increasing compression (decreasing l) the noise level increases, but no clear underlying dynamics is found until at $l \lesssim 3.2$ Å $p(x < 0)$ starts to oscillate around a value of 0.5 with decreasing wavelength. At $l \lesssim 2.7$ Å the amplitude of $p(x < 0)$ suddenly collapses and no further dynamics is observed.

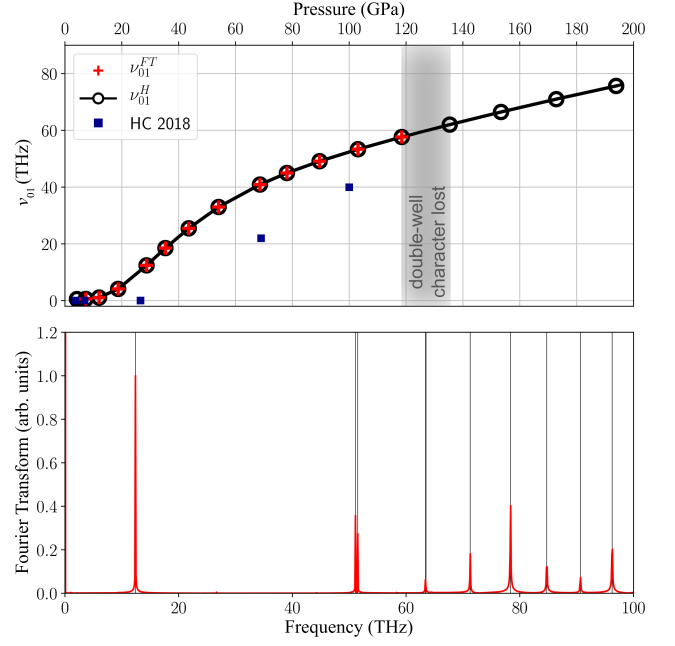


FIG. 5. Results of the dynamical calculation for the hexagonal configuration. **(bottom)** Transition frequency spectrum calculated from the eigenvalues of the Hamiltonian (black vertical lines) and the solution to the dynamic problem, represented by the Fourier transformation of the probability of finding the proton in the left side of the potential, $p(k)$, with amplitudes normalized to ν_{01}^H (red) for $l = 2.95$ Å. **(top)** ν_{01}^{FT} from the eigenvalue analysis (black circles) and position of ν_{01}^{FT} in $p(k)$ (red crosses) as a function of P . Blue squares show hydrogen jump rates calculated by Hernandez and Caracas²⁵ (HC 2018) on the basis of molecular dynamics simulations.

B. Pressure dependence

The frequency ν_{01}^H , calculated from the eigenvalues, increases continuously with P in a square root-like fashion between 5 and ~ 100 -120 GPa and linearly upon further P -increase to our maximum $P \approx 200$ GPa (Fig. 5 for the hexagonal configuration), indicating that there is no structural phase transition of first or second order. This change in slope indicates a change in dynamic behavior independent of the particular form of the initial state, providing an additional (although less sensitive) analysis tool, and shows that the exact form of Ψ , in particular the use of \mathcal{F} , only improves the analysis, but is not required.

ν_{01}^{FT} , calculated from $p(k)$, follows this trend to $P \lesssim 130$ GPa, where we find a significant drop in amplitude (Fig. 6), suggesting that the ν_{01} oscillation is no longer contributing to the dynamics of the system.

Proton jump frequencies calculated by Hernandez and Caracas²⁵ are in quantitative agreement with our results for the hexagonal configuration, but shifted to slightly higher P , which is most likely a consequence of their classical treatment of the problem. The occupation of

ν_{01}^{FT} for the ice-rule violating configuration drops at a lower P (Fig. 6), reflecting the earlier transition to a single-well potential (Fig. 3).

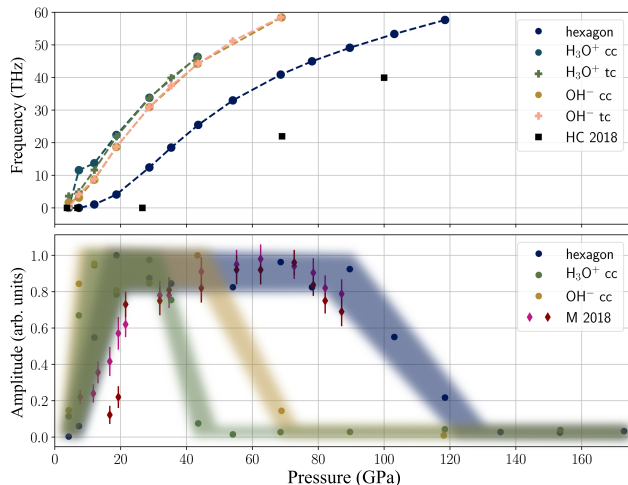


FIG. 6. **(top)** Excitation frequencies ν_{01}^{FT} as a function of P at 300 K for the different proton configurations explored in this study. Black squares show hydrogen jump rates calculated by Hernandez and Caracas²⁵ (HC 2018) on the basis of molecular dynamics simulations. **(bottom)** Corresponding amplitudes of ν_{01}^{FT} in $p(k)$. Amplitudes are normalized to the maximum value for the respective configuration³⁵. Diamonds in magenta and purple show the result of a peak analysis of NMR experiments by Meier *et al.*²⁶ (M 2018).

V. DISCUSSION & CONCLUSION

If we compare the amplitude of ν_{01}^{FT} in $p(k)$ as a function of P with the NMR line shape analysis by Meier *et al.*²⁶ (Fig. 6), we find that the hexagonal configuration reproduces the P -dependence of the NMR data at room T well: A strong increase in amplitude up to $P \sim 20$ GPa, a plateau to $P \sim 80 - 90$ GPa, and a subsequent drop. This supports the interpretation of Lin *et al.*²¹ that charge balance tends to be maintained at low T , and therefore tunneling is correlated, represented by the hexagonal configuration.

We do not find a sharp phase transition in cubic ice between the emergence of ice-VII at ~ 2 GPa and 200 GPa, well in the stability field of ice-X, but a gradual change from a double- to a single-well potential, and we predict related changes in proton dynamics. Based on our results we can distinguish regions of characteristic proton dynamics and potential (at room T):

- (i) For $2 \text{ GPa} < P < 20 \text{ GPa}$, protons become increasingly delocalized, as the potential barrier decreases;
- (ii) for $20 \text{ GPa} < P < 90 \text{ GPa}$, protons tunnel in a fashion well represented by correlated hexagons;

(iii) for $90 \text{ GPa} < P < 130 \text{ GPa}$, symmetrization occurs and the amplitude of ν_{01}^{FT} drops significantly as the potential barrier becomes small, but non-zero;

(iv) for $P \gtrsim 130 \text{ GPa}$, the potential is fully symmetric and no proton dynamics is expected for an initially symmetric state.

In P -ranges (i) and (iii), varying energy and momentum transfer to the sample by different experimental methods may modify the probed potential, ranging from an excitation of the proton spin system without significant momentum or energy transfer to the lattice in NMR²⁶, through momentum transfer by collisions with neutrons²⁴, the excitation of lattice vibrations in Raman³⁰⁻³², infrared¹⁰ and Brillouin^{19,36-38} spectroscopy, to high-energy irradiation with X-rays^{12,15,28,29}.

The onset of tunneling in P -range (i), predicted in our simulations, can be directly linked to low- P features found in X-ray diffraction^{12,15,28}, but appears to be absent^{10,19} or only weakly visible^{32,38} in lattice vibration-based methods. As thermal energy would couple most directly to the phonons, this absence supports the argument that potential parameters and therefore the onset of tunneling does not strongly depend on T . Instead, optical methods^{10,19,30,32} find anomalies at $P \approx 40$ GPa which suggests that momentum transfer interacts with the lattice in a fashion not visible in the ground-state calculations at the basis of our potentials. Features at $P \gtrsim 60$ GPa, found in X-ray diffraction^{12,15,28,29} and optical measurements^{10,19,32} correlate with the highest mobility in the NMR data²⁶ (Fig. 4), indicating that compressional energy added to the system can no longer be transferred to the protons.

Optical^{19,30} and X-ray diffraction studies²⁹ are in line with our interpretation of P -range (iii), with structural changes at $P \gtrsim 80$ GPa and $P \approx 110$ GPa, respectively. The lower symmetrization P in the optical experiments^{19,30} supports the argument that momentum transfer may suppress correlated tunneling. The symmetrization P from the X-ray diffraction experiments²⁹ is in good agreement with our prediction, and the cessation of dynamics extrapolated from the NMR results²⁶.

Based on this observation we suggest that experimental methods can be expected not to agree on a single transition P in a system like H_2O ice. Further, the limited experimental resolution in terms of P -sampling may lead to an over-interpretation of the nature of the phase transition, in some cases claiming sharp transitions^{19,28,29}.

ACKNOWLEDGEMENTS

FT and GSN were supported by Deutsche Forschungsgemeinschaft (DFG) within FOR 2440 (Matter under Planetary Interior Conditions) with grant STE1105/13-1 and TM with grant ME5206/3-1. We thank F. Ungar

(TP III, Universität Bayreuth) for very helpful discussions. Computations were partly performed at the Leibniz Supercomputing Centre of the Bavarian Academy of

Sciences and the Humanities. GPU accelerated computations are supported by the NVIDIA Corporation with the donation of a Titan Xp GPU.

-
- * f.trybel@uni-bayreuth.de
- ¹ O. Tschauner, S. Huang, E. Greenberg, V. B. Prakapenka, C. Ma, G. R. Rossman, A. H. Shen, D. Zhang, M. Newville, A. Lanzirotti, and K. Tait, *Science* **359**, 1136 (2018).
 - ² F. Nimmo and R. T. Pappalardo, *Journal of Geophysical Research: Planets* **121**, 1378 (2016).
 - ³ M. K. Dougherty and L. J. Spilker, *Reports on Progress in Physics* **81**, 065901 (2018).
 - ⁴ D. Valencia, D. D. Sasselov, and R. J. O’Connell, *The Astrophysical Journal* **665**, 1413–1420 (2007).
 - ⁵ J. Monteux, G. J. Golabek, D. C. Rubie, G. Tobie, and E. D. Young, *Space Science Reviews* **214**, 39 (2018).
 - ⁶ See Supplemental Material at [URL will be inserted by publisher] for details of the tunnelling calculations and the respective potentials as well as additional figures.
 - ⁷ J. D. Bernal and R. H. Fowler, *The Journal of Chemical Physics* **1**, 515 (1933).
 - ⁸ A. Polian and M. Grimsditch, *Phys. Rev. Lett.* **52**, 1312 (1984).
 - ⁹ C. Lee, D. Vanderbilt, K. Laasonen, R. Car, and M. Parrinello, *Phys. Rev. B* **47**, 4863 (1993).
 - ¹⁰ A. F. Goncharov, V. V. Struzhkin, M. S. Somayazulu, R. J. Hemley, and H. K. Mao, *Science* **273**, 218 (1996).
 - ¹¹ K. Aoki, H. Yamawaki, M. Sakashita, and H. Fujihisa, *Phys. Rev. B* **54**, 15673 (1996).
 - ¹² E. Wolanin, P. Pruzan, J. C. Chervin, B. Canny, M. Gauthier, D. Häusermann, and M. Hanfland, *Phys. Rev. B* **56**, 5781 (1997).
 - ¹³ M. Bernasconi, P. L. Silvestrelli, and M. Parrinello, *Phys. Rev. Lett.* **81**, 1235 (1998).
 - ¹⁴ M. Benoit, D. Marx, and M. Parrinello, *Nature* **392**, 258 (1998).
 - ¹⁵ P. Loubeyre, R. LeToullec, E. Wolanin, M. Hanfland, and D. Häusermann, *Nature* **397**, 503 (1999).
 - ¹⁶ M. Benoit, A. H. Romero, and D. Marx, *Phys. Rev. Lett.* **89**, 145501 (2002).
 - ¹⁷ E. Sanz, C. Vega, J. L. F. Abascal, and L. G. MacDowell, *Phys. Rev. Lett.* **92**, 255701 (2004).
 - ¹⁸ R. Caracas, *Phys. Rev. Lett.* **101**, 085502 (2008).
 - ¹⁹ Y. Asahara, K. Hirose, Y. Ohishi, N. Hirao, and M. Murakami, *Earth and Planetary Science Letters* **299**, 474 (2010).
 - ²⁰ X. Z. Lu, Y. Zhang, P. Zhao, and S. J. Fang, *The Journal of Physical Chemistry B* **115**, 71 (2011).
 - ²¹ L. Lin, J. A. Morrone, and R. Car, *Journal of Statistical Physics* **145**, 365 (2011).
 - ²² M. French and R. Redmer, *Phys. Rev. B* **91**, 014308 (2015).
 - ²³ J. Tsuchiya and T. Tsuchiya, *The Journal of Chemical Physics* **146**, 014501 (2017).
 - ²⁴ S. Klotz, K. Komatsu, H. Kagi, K. Kunc, A. Sano-Furukawa, S. Machida, and T. Hattori, *Phys. Rev. B* **95**, 174111 (2017).
 - ²⁵ J.-A. Hernandez and R. Caracas, *The Journal of Chemical Physics* **148**, 214501 (2018).
 - ²⁶ T. Meier, S. Petitgirard, S. Khandarkhaeva, and L. Dubrovinsky, *Nature Communications* **9**, 2766 (2018).
 - ²⁷ C. Drechsel-Grau and D. Marx, *Physical Chemistry Chemical Physics* **19**, 2623 (2017).
 - ²⁸ M. Somayazulu, J. Shu, C.-s. Zha, A. F. Goncharov, O. Tschauner, H.-k. Mao, and R. J. Hemley, *The Journal of Chemical Physics* **128**, 064510 (2008).
 - ²⁹ E. Sugimura, T. Iitaka, K. Hirose, K. Kawamura, N. Sata, and Y. Ohishi, *Phys. Rev. B* **77**, 214103 (2008).
 - ³⁰ K. R. Hirsch and W. B. Holzapfel, *The Journal of Chemical Physics* **84**, 2771 (1986).
 - ³¹ P. Pruzan, J. C. Chervin, E. Wolanin, B. Canny, M. Gauthier, and M. Hanfland, *Journal of Raman Spectroscopy* **34**, 591 (2003).
 - ³² C.-S. Zha, J. S. Tse, and W. A. Bassett, *The Journal of Chemical Physics* **145**, 124315 (2016).
 - ³³ K. O. Friedrichs, *Transactions of the American Mathematical Society* **55**, 132 (1944).
 - ³⁴ The potential for the collective movement of all protons is not evaluated as the combined energy barrier of all protons in the system is significantly higher than for the hexagonal collective movement.
 - ³⁵ For the hexagonal configuration, the point at $l = 2.85 \text{ \AA}$ is missing, as the peak in the spectrum is not sufficiently resolved by the discrete calculation grid.
 - ³⁶ M. Ahart, M. Somayazulu, S. A. Gramsch, R. Boehler, H.-k. Mao, and R. J. Hemley, *The Journal of Chemical Physics* **134**, 124517 (2011).
 - ³⁷ J. S. Zhang, M. Hao, Z. Ren, and B. Chen, *Applied Physics Letters* **114**, 191903 (2019).
 - ³⁸ X. Li, W. Shi, X. Liu, and Z. Mao, *American Mineralogist: Journal of Earth and Planetary Materials* **104**, 1307 (2019).
 - ³⁹ P. Giannozzi, S. Baroni, N. Bonini, M. Calandra, R. Car, C. Cavazzoni, D. Ceresoli, G. L. Chiarotti, M. Cococcioni, I. Dabo, A. Dal Corso, S. de Gironcoli, S. Fabris, G. Fratesi, R. Gebauer, U. Gerstmann, C. Gougousis, A. Kokalj, M. Lazzeri, L. Martin-Samos, N. Marzari, F. Mauri, R. Mazzarello, S. Paolini, A. Pasquarello, L. Paulatto, C. Sbraccia, S. Scandolo, G. Sclauzero, A. P. Seitsonen, A. Smogunov, P. Umari, and R. M. Wentzcovitch, *Journal of Physics: Condensed Matter* **21**, 395502 (2009).
 - ⁴⁰ P. Giannozzi, O. Andreussi, T. Brumme, O. Bunau, M. B. Nardelli, M. Calandra, R. Car, C. Cavazzoni, D. Ceresoli, M. Cococcioni, N. Colonna, I. Carnimeo, A. D. Corso, S. de Gironcoli, P. Delugas, R. A. D. Jr., A. Ferretti, A. Floris, G. Fratesi, G. Fugallo, R. Gebauer, U. Gerstmann, F. Giustino, T. Gorni, J. Jia, M. Kawamura, H.-Y. Ko, A. Kokalj, E. Küçükbenli, M. Lazzeri, M. Marsili, N. Marzari, F. Mauri, N. L. Nguyen, H.-V. Nguyen, A. O. de-la Roza, L. Paulatto, S. Poncé, D. Rocca, R. Sabatini, B. Santra, M. Schlipf, A. P. Seitsonen, A. Smogunov, I. Timrov, T. Thonhauser, P. Umari, N. Vast, X. Wu, and S. Baroni, *Journal of Physics: Condensed Matter* **29**, 465901 (2017).

- ⁴¹ J. Romero, E. Phillips, G. Ruetsch, M. Fatica, F. Spiga, and P. Giannozzi, in *High Performance Computing Systems. Performance Modeling, Benchmarking, and Simulation, Lecture Notes in Computer Science*, Vol. 10724, edited by S. Jarvis, S. Wright, and S. Hammond, 67-87 (2018).
- ⁴² A. D. Becke, Phys. Rev. A **38**, 3098 (1988).
- ⁴³ M. Dion, H. Rydberg, E. Schröder, D. C. Langreth, and B. I. Lundqvist, Phys. Rev. Lett. **92**, 246401 (2004).
- ⁴⁴ T. Thonhauser, V. R. Cooper, S. Li, A. Puzder, P. Hyldgaard, and D. C. Langreth, Phys. Rev. B **76**, 125112 (2007).
- ⁴⁵ D. C. Langreth, B. I. Lundqvist, S. D. Chakarova-Käck, V. R. Cooper, M. Dion, P. Hyldgaard, A. Kelkkanen, J. Kleis, L. Kong, S. Li, *et al.*, Journal of Physics: Condensed Matter **21**, 084203 (2009).
- ⁴⁶ J. Klimeš, D. R. Bowler, and A. Michaelides, Journal of Physics: Condensed Matter **22**, 022201 (2010).
- ⁴⁷ T. Thonhauser, S. Zuluaga, C. A. Arter, K. Berland, E. Schröder, and P. Hyldgaard, Phys. Rev. Lett. **115**, 136402 (2015).
- ⁴⁸ K. Berland, V. R. Cooper, K. Lee, E. Schröder, T. Thonhauser, P. Hyldgaard, and B. I. Lundqvist, Reports on Progress in Physics **78**, 066501 (2015).
- ⁴⁹ M. J. Gillan, D. Alfè, and A. Michaelides, The Journal of Chemical Physics **144**, 130901 (2016).
- ⁵⁰ J. P. Perdew, K. Burke, and M. Ernzerhof, Phys. Rev. Lett. **77**, 3865 (1996).
- ⁵¹ H. J. Monkhorst and J. D. Pack, Phys. Rev. B **13**, 5188 (1976).
- ⁵² K. Momma and F. Izumi, Journal of Applied Crystallography **44**, 1272 (2011).